Article

Improved Mechanical Properties of SUS304/AA5083 Dissimilar Joint by Laser Ablation Pretreatment in Vortex- Friction Stir Lap Welding

Xiaochao Liu [ID], Jingyue Luo, Wenhui Bao, Xianjun Pei *, Qinghua Wang [ID] and Zhonghua Ni

School of Mechanical Engineering, Southeast University, Nanjing 211189, China; xcliu1990@seu.edu.cn (X.L.); qinghua-wang@seu.edu.cn (Q.W.)
* Correspondence: xpei@seu.edu.cn; Tel.: +86-025-52090501

Abstract: To obtain a high-quality Al/steel dissimilar joint, a micro-groove-assisted vortex-friction stir lap welding (MG-VFSLW) process was developed. Through prefabricating micro-grooves on the steel plate surface by laser ablation, high-quality mechanical interlock and metallurgical bonding were obtained simultaneously in the MG-VFSLW process. The weld formation, interface microstructure, mechanical properties, and failure mode in MG-VFSLW were studied by comparing them with those in VFSLW. The results showed that a line load of the AA5083/SUS304 dissimilar joint up to 485.9 N/mm was obtained by MG-VFSLW, which is 40.1% higher than that in VFSLW. Remarkable intermetallic compound layers and cracks were found in VFSLW. The cracks were closely related to the oxides on the interface. However, in MG-VFSLW, cross-riveting aluminum rivets and steel rivets were formed on the interface due to the micro-grooves and flashes made by the laser ablation. Good metallurgical bonding was also formed between AA5083 and SUS304. No remarkable intermetallic compound layers and cracks occurred. During the tensile shear tests, the aluminum rivets were cut off and some dimples and tear ridges existed on the fracture surface. In short, the high strength of the Al/steel lap joint in MG-VFSLW was attributed to the high-quality mechanical interlock and metallurgical bonding.

Keywords: Al/steel dissimilar joining; friction stir lap welding; vortex material flow; mechanical interlock; mechanical properties; laser ablation

1. Introduction

Dissimilar material joining is becoming more and more important for the lightweight and multi-function aspects of high-end equipment manufacturing [1,2]. It has been in great demand in aerospace, electric vehicles, hydrogen energy, etc. For example, the Al/steel dissimilar joint has the advantages both of high specific strength, good corrosion resistance, and the low density of aluminum alloys, and of the high strength and low cost of steels, which can be used in automotive bodies [3], high-pressure hydrogen storage tanks [4], rocket fuel storage tanks [5], and so on.

Currently, there are mainly three kinds of methods for Al/steel dissimilar joining. One is welding–brazing, in which lasers [6,7], arcs [8–10], plasma arcs [11], or their hybrids [12–14] are used as the heating source to melt aluminum, and the melted aluminum is spread onto the solid steel to form a brazed joint by solidification. However, brittle iron–aluminum intermetallic compounds (IMCs) are easily formed during the melting–solidification process [6–14], resulting in relatively low strength of the brazed Al/steel joint. The second is riveting [15,16], which can obtain high joint strength but the gas tightness is inadequate in some applications such as storage tanks. The third is solid-state welding, including friction-based welding [17,18], diffusion welding [19,20], and explosion welding [21], among which friction stir welding (FSW) is believed to be a promising weld-

ing method for Al/steel dissimilar joining due to its high quality, wide adaptability, and flexibility [22,23].

There have been many studies on the FSW of Al/steel dissimilar joining. The most common types of Al/steel dissimilar FSW joints are butt joints and lap joints. In the FSW of Al/steel dissimilar butt joints, the tool is usually offset to the aluminum side [24,25]. Only a slight touch occurs between the FSW tool and the steel. However, this touch still leads to the wear of the tool, and a part of the steel will be fragmentized and brought into the aluminum, forming defects [26]. In addition, owing to the high friction heat generation rate between the tool and the steel, some brittle iron–aluminum IMCs are generally formed on the Al/steel interface [27,28]. The control of IMCs is the most important issue in the FSW process of Al/steel dissimilar joining. Adjusting welding parameters [24–29] such as the welding speed, rotating speed, tilt angle, etc., changing the tool design [25], or inserting an interlayer [30] has been widely used to control the IMCs and to optimize the mechanical properties of the Al/steel butt joint. Recently, Zhang et al. [31] reported a new FSW butted method with no contact between the tool and the steel plate, in which a thickened Al alloy plate was applied to avoid the tool touching the steel plate.

For the FSW of the lap joint of Al/steel, the aluminum plate is usually put on the steel plate, and the tool's pin is slightly inserted into the steel plate [32]. Therefore, tool wear and iron–aluminum IMCs in friction stir lap welding (FSLW) are also inescapable. Many attempts have been made to overcome the inherent issues of the Al/steel FSLW. For example, Wan and Huang [33] proposed a tool with a convex pin tip to realize the control of the interfacial structures. Zhou et al. [34] used an Al interlayer fabricated by friction surfacing to assist the FSLW (FSaFSLW) of Al/steel to avoid the tool being inserted into the steel plate and thus eliminate the tool wear. Huang et al. [35] designed a tool with an enlarged pin tip and circumferential notches shape to eliminate the hook defect and enhance the interface deformation effect in the FSLW of dissimilar materials. Liu et al. [36] used the ultrasonic vibration enhanced friction stir welding (UVeFSW) process to improve the bonding quality of Al/steel by enhancing the mechanical interlocking ability and changing the type and thickness of the IMC layer. Wang et al. [37] developed a double-pass welding method to optimize the strength of the Al/steel lap welds. Recently, Liu et al. [38,39] put forward a joining method of Al/steel via FSLW with no contact between the tool and the steel plate. The tool's pin needs to be inserted into the aluminum plate and kept only 0.1 mm away from the surface of the steel plate. Good mechanical properties can be obtained under this condition because the nanoscale amorphous metal is developed at the Al/steel interface. To overcome the difficulty of the control of the plunging depth of the tool, Luo et al. [40] proposed a vortex-friction stir lap welding (VFSLW) process. This process referenced the vortex-friction stir welding (VFSW) process, which was developed by the authors' group [41–44]. In VFSLW, a hole is made from the conventional FSW tool's pin tip and an aluminum bar owning identical material to the workpiece is inserted into the hole, and then the conventional FSLW procedure is conducted. In this way, a vortex material flow is formed under the pin tip, which rubs the surface of the steel plate and then a diffusion bonding is formed. However, metallurgical bonding alone is not enough to obtain high strength and fatigue resistance. Huang et al. [45] developed a self-riveting FSLW (SR-FSLW) process of Al/steel to improve the bonding strength. Unfortunately, no metallurgical bonding occurred on the riveting interface. The rivet part easily dropped off during the loading process.

In this study, a high-quality Al/steel dissimilar joint based on metallurgical bonding and mechanical interlock was fabricated by combining the VFSLW process and prefabricating micro-grooves on the steel surface by laser ablation pretreatment. This novel process is called micro-groove-assisted VFSLW, hereinafter referred to as MG-VFSLW. The weld formation, interface microstructure, mechanical properties and failure mode were studied by comparing them with those in conventional VFSLW. This study provides new thinking to improve the mechanical properties of Al/steel dissimilar joints.

2. Materials and Methods

2.1. Materials

In this study, 5083-H112 aluminum alloy and SUS304 stainless steel were used as the base materials. Their chemical compositions are shown in Tables 1 and 2, respectively. Both the supplied AA5083 and SUS304 plates were 3 mm in thickness. They were cut into small pieces with dimensions of 200 mm in length and 120 mm in width. The measured microhardness of AA5083 and SUS304 was ~82 Hv and ~200 Hv, respectively. The FSW tool was made of H13 tool steel. The aluminum bar inserted into the FSW tool was made of AA5083.

Table 1. Chemical composition of 5083 aluminum alloy (wt. %).

Si	Fe	Cu	Mg	Zn	Ti	Mn	Cr	Al
0.40	0.40	0.10	4.50	0.25	0.15	0.60	0.15	Bal.

Table 2. Chemical composition of 304 stainless steel (wt. %).

C	S	P	Si	Mn	Cr	Ni	N	Fe
0.08	0.03	0.045	0.75	2.0	18–20	8~10.5	0.1	Bal.

2.2. Process Parameters

The process parameters in this study mainly involve three aspects, i.e., the parameters of the tool, the welding parameters and the parameters of the micro-grooves.

The tool used in this study is shown in Figure 1. It consisted of a shoulder with concave concentric rings, a threaded pin, and an aluminum bar (or called stir bar) that was inserted into the tool from the pin tip and was fixed on the holder by two set screws. The shoulder diameter was 20 mm. The threaded pin had a truncated cone shape with a thread pitch of 1 mm. The diameters of the pin at the two ends were 12 mm and 10 mm, respectively. The length of the pin was 2.6 mm. The diameter of the aluminum bar was 8 mm.
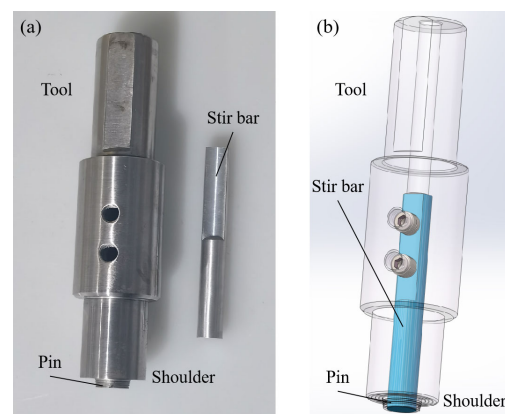
Figure 1. The tool used in the vortex-friction stir lap welding: (**a**) image; (**b**) 3D view.

The welding parameters for conventional VFSLW and MG-VFSLW were the same. The rotation speed was 500 rpm, the welding speed was 15 mm/min, and the tilt angle of the tool was 2.5°. The plunge depth of the shoulder was 0.1 mm, which resulted in a distance of 0.3 mm between the pin tip and the steel plate. As a result, the tool did not come into contact with the steel plate, and thus there was no need to use harder tools as in the conventional FSW of steel. The type of FSW machine used in this study was the HT-JM16×8/1, manufactured by Aerospace Engineering Equipment (Suzhou, China) Co., Ltd.

Figure 2 shows the morphology and geometry of the micro-grooves made by laser ablation. The micro-grooves were parallel distributed. The average depth of the micro-grooves was ~50 μm. The height of the flash was nearly 25 μm. The separation distance of two adjacent micro-grooves was 100 μm. The type of pulsed fiber laser used in this study was the YDFLP-E-60-M7-M-R, manufactured by Shenzhen Opto-electronics Co., Ltd. (Shenzhen, China). The laser power was 6.5 W, the laser scanning speed was 300 mm/s, the scanning frequency was 40 kHz, and the scan times were 30.
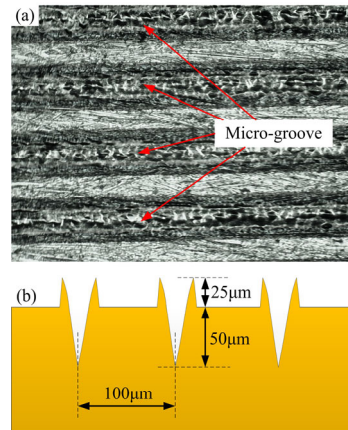
Figure 2. Morphology (**a**) and geometry (**b**) of the micro-grooves made by laser ablation.

2.3. Experimental Procedure

The schematic of the MG-VFSLW process is shown in Figure 3. Before welding, the oxides on the surfaces of AA5083 and SUS304 were first removed by mechanical grinding. The workpieces were sanded with a wire brush grinder. After grinding, the dark oxide layer on the surface of the workpiece was replaced by fresh metal and became rich in metallic luster. Then a series of micro-grooves were prefabricated on the SUS304 surface by laser ablation along the welding direction. After laser ablation, an acid pickling process was conducted using a 5% HCl solution for the micro-grooves. Next, we put the AA5083 plate on the SUS304 plate and covered the micro-grooves. Finally, we used the process parameters mentioned above to finish the welding procedure.
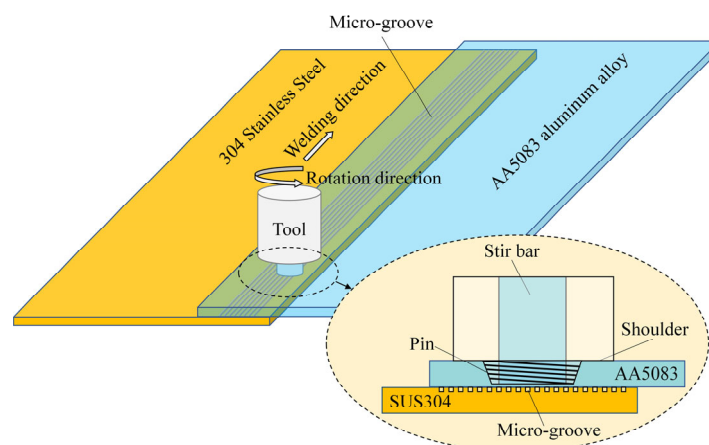
Figure 3. Schematic of the micro-groove-assisted vortex-friction stir lap welding.

After welding, the weld formation was checked by surface and cross-section inspections. The mechanical properties of the Al/steel dissimilar joint were evaluated by a tensile shear test and a Vickers hardness test. Three tensile specimens and one metallographic specimen were taken perpendicular to the welding direction, as shown in Figure 4a. The metallographic specimens were prepared by hand polishing and etching with a Keller's reagent comprising 2.5% nitric acid, 1.5% hydrochloric acid, 1.0% hydrofluoric acid, and

95% H_2O. During the tensile shear test, two compensation gaskets were used to ensure that the bonding interface bore only a parallel shearing force, as shown in Figure 4b. The tensile shear test was conducted on a universal testing machine with a maximum load of 100 kN (UTM5105) with a constant cross-head speed of 2 mm/min. The Vickers hardness was measured on the cross-section of the weld using a micro-hardness tester (MHVS-1000Z). For SUS304 and AA5083, the microhardness was measured along the parallel lines 0.2 mm and 0.5 mm away from the Al/steel interface with an interval of 1 mm, respectively. The loads used for SUS304 and AA5083 were 1.0 Kgf and 0.5 Kgf with 10 s dwell time, respectively. The microstructure of the Al/steel interface and the fracture surface was characterized by a field emission SEM (FEI Nova Nano SEM450). No etching was made before the SEM observation.
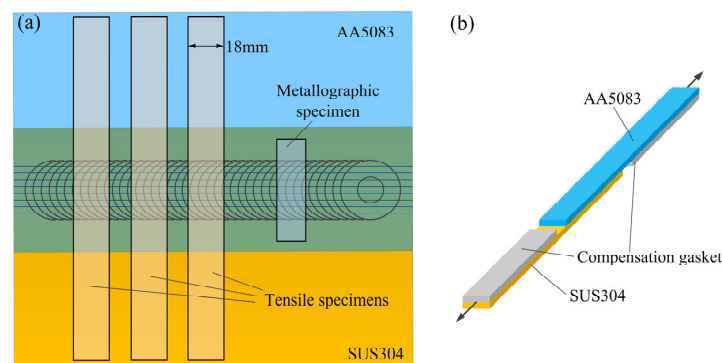
Figure 4. Schematic drawing of the weld evaluation: (**a**) sampling positions; (**b**) tensile shear specimen configuration.

3. Results and Discussion

3.1. Weld Formation

The weld surface morphologies obtained by VFSLW and MG-VFSLW are shown in Figure 5a and b, respectively. There is no obvious difference between them, indicating that the micro-grooves did not interfere with the welding surface formation.
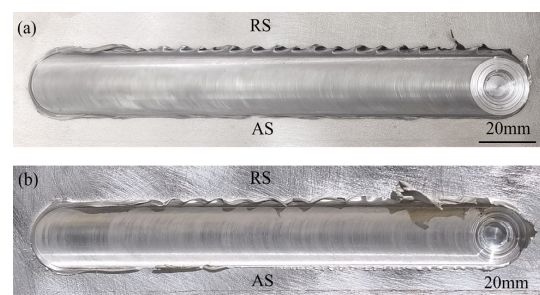
Figure 5. Weld surface morphologies obtained by VFSLW (**a**) and MG-VFSLW (**b**).

The weld macro cross-sections of the VFSLW and MG-VFSLW specimens are shown in Figure 6a and b, respectively. There is no macro void defect or crack in either the VFSLW or the MG-VFSLW specimen. Both of the stir zones are visible. In the stir zone, an "onion ring" structure, which is a typical characteristic of conventional FSW welds, exists. This indicates that VFSLW can work like conventional FSW although an aluminum bar is inserted into the FSW tool. In addition, the Al/steel interface is very straight. This is because the pin tip is 0.3 mm away from the steel surface. No friction occurred between the tool and the steel. Only the vortex material flow induced by the aluminum bar together with the pin rubbed the steel surface. In the MG-VFSLW weld, the micro-grooves were found as shown in Figure 6b. They were uniformly distributed beneath the stir zone.
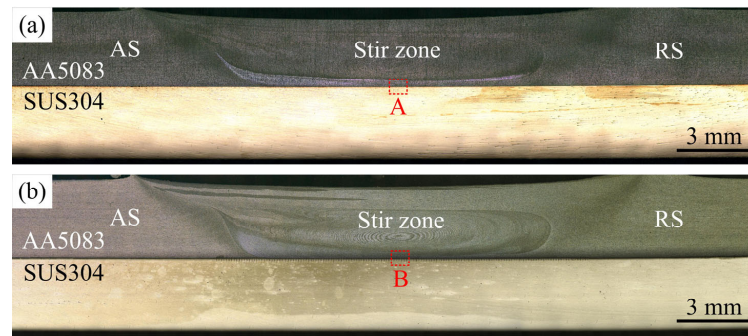
Figure 6. Weld macro cross-sections obtained by VFSLW (**a**) and MG-VFSLW (**b**).

3.2. Interface Microstructure

The microstructure of the Al/steel interface obtained by conventional VFSLW is shown in Figure 7. It corresponds to area A in Figure 6a. From Figure 7a, a thin layer of material was seen on the interface, which had a different gray level from SUS304 and AA5083. These are known as IMCs, which usually occur in dissimilar materials joining [23–35]. The existence of the IMCs shows that the vortex material flow was strong enough to rub the steel surface and generate enough heat. To further observe the morphology of the IMCs, the magnified figures of the local areas b–d in Figure 7a were taken and shown in Figure 7b–d. It can be seen that the thickness of the IMCs ranges from 1.20 to 1.97 μm. In addition, some cracks can be found in the magnified figures, which are located close to SUS304 (Figure 7b) or close to AA5083 (Figure 7d). They were not continuous. For example, no crack was seen in Figure 7c. To recognize the IMCs, the spectrums of points 1 and 2 in Figure 7b are listed in Table 3. The atom ratios of the Fe/Al are approximately equal to 2:9 in the center of the IMC layer and 1:1 close to the SUS304 side. To further analyze the IMCs on the Al/steel interface, the scanning maps of the elements Fe, Al, O, Cr, and Mg by EDS are shown in Figure 8. The location of the IMCs was marked on the element maps by white dotted lines according to the SEM image. It can be seen that the IMCs mainly consist of Fe, Al, and Cr. Close to the SUS304 side, the content of the Al element is remarkably decreased in the IMC layer, which is replaced by Fe and Cr. According to the spectrum in Table 3, it was inferred that the IMC was FeAl [46]. At the center of the IMC layer, the contents of Fe and Al are almost constant, which was inferred as Fe_2Al_9 [47], according to Table 3. Near the AA5083 side, the elements of O and Mg were segregated along the boundary of the IMCs. A similar phenomenon has been reported by Liu et al. [39].
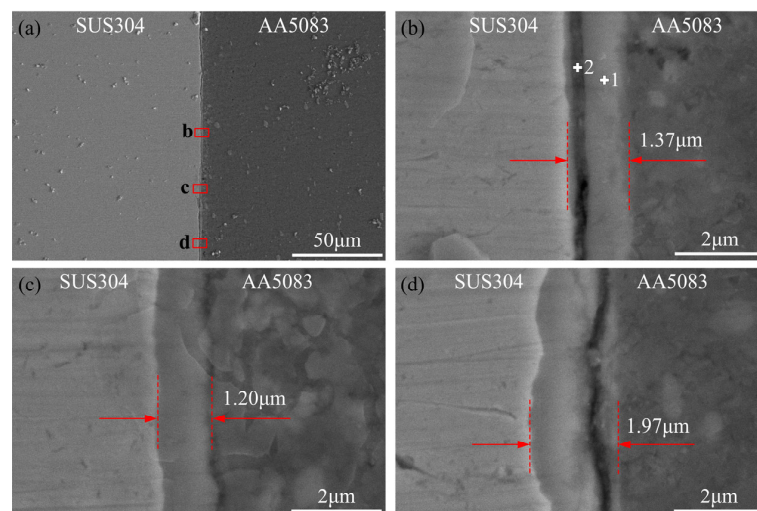
Figure 7. SEM images showing the microstructure of the Al/steel interface in VFSLW: (**a**) overview of the interface; (**b–d**) high-resolution images of the local regions b–d in (**a**).

Table 3. The EDS results of the IMC layer at points 1 and 2 shown in Figure 7b (at %).

Element (at. %)	Al	Fe	Cr	Mg	O
Point 1	70.45	16.10	4.43	2.47	6.55
Point 2	38	42.25	10.64	0.47	8.43
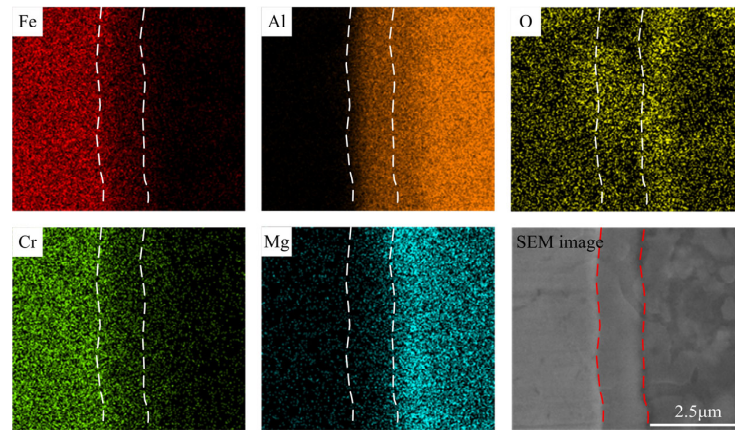
Figure 8. Element distribution maps of the interface in Figure 7c obtained by EDS analysis.

To further analyze the changes in the element content, the EDS analysis results of the linear scanning across the IMCs are shown in Figure 9. In Figure 9a, it can be seen that a flat segment exists in the distribution of the Al element, meaning that IMCs with a uniform composition were formed. This has been inferred to be Fe_2Al_9 hereinbefore. In addition, the O element was segregated at both sides of the IMCs. The Mg element was segregated only at the AA5083 side. The segregation of the O element may be caused by the oxidation of the base materials before and during welding. For the segregation of the Mg element, since Mg and Fe (or Cr) do not dissolve each other, the Mg atoms remained when the iron–aluminum IMCs were formed. Figure 9b shows the element changes when the crack occurred near the AA5083 side. It can be found that the Mg and O elements were segregated significantly near the crack. It is thus inferred that the crack near the AA5083 side may be caused by MgO. In Figure 9c, the crack is close to the SUS304 side. Near the crack, only the segregation of the O element was formed. This indicates that the crack may be caused by $(Fe, Cr) O_x$. In other words, the cracks formed along the IMC layer were caused by metallic oxides. They may be eliminated by carefully removing the oxides before welding and isolating the air during welding.
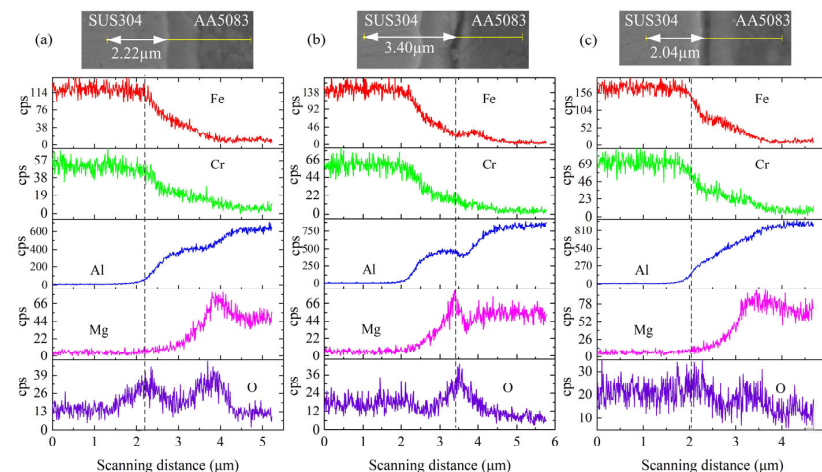
Figure 9. EDS linear scanning results across the IMCs: (**a**) no crack; (**b**) crack close to AA5083; (**c**) crack close to SUS304.

Figure 10 shows the microstructure of the Al/steel interface obtained by the MG-VFSLW process corresponding to area B in Figure 6b. In Figure 10a, it can be seen clearly that the micro-grooves were filled by the AA5083 aluminum alloy. A typical micro-groove is shown in Figure 10b. It is the magnified figure of region b in Figure 10a. A good mechanical interlock was formed between SUS304 and AA5083. It can be seen that an aluminum rivet was inserted into SUS304, and two steel rivets were inserted into AA5083. The aluminum rivet corresponds to the micro-groove made by laser ablation, while the steel rivet corresponds to the flash formed during laser ablation. To observe the Al/steel interface, magnified regions c and d in Figure 10b are shown in Figure 10c,d. Differently from the scene seen in VFSLW (Figure 7), no visible IMC was formed on the two interfaces. However, it is not excluded that the nanoscale IMC or amorphous was formed at the Al/steel interface [31,38,39]. This means that the micro-grooves suppressed the formation IMCs during the VFSLW process under the current experimental condition. The mechanism can be understood as follows: owing to the existence of the micro-grooves, the plastic-flow materials will enter into the micro-grooves during the welding process and thus the frictional pressure will be decreased. This leads to the heat generation rate decreasing. Therefore, the formation of IMCs is suppressed.
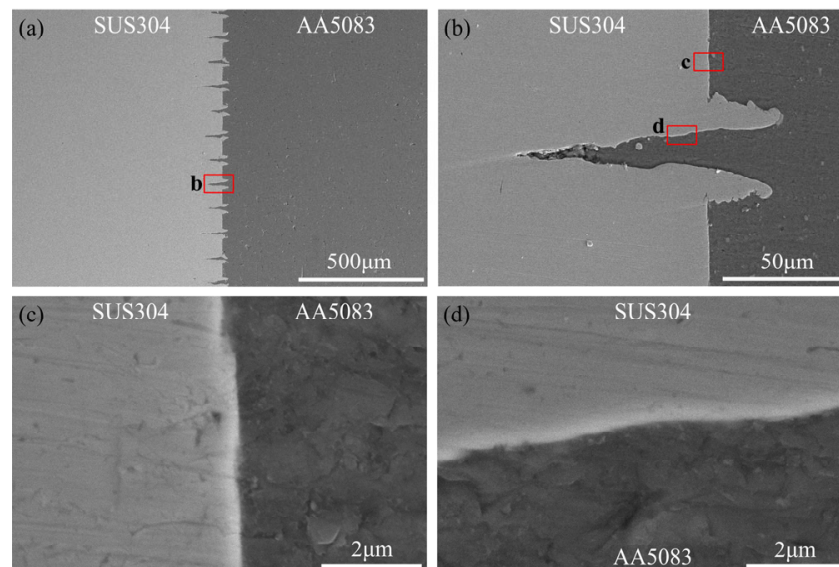
Figure 10. SEM images showing the microstructure of the Al/steel interface in MG-VFSLW: (**a**) overview of the interface; (**b**–**d**) the magnified figure of the area marked b in (**a**); (**c**,**d**) the magnified figures of the areas marked c and d in (**b**).

To further characterize the Al/steel interfaces in MG-VFSLW, the linear scanning results obtained by EDS analysis are shown in Figure 11. Figure 11a–c shows the changes in the element content across the steel rivet, the aluminum rivet, and the straight Al/steel interface, respectively. The specific locations of the linear scanning are shown in Figure 11d. From Figure 11a–c, the changes in the content of the elements (Al, Mg, Fe, Cr) are gradually varied. No flat segment existed during the transitions either from AA5083 to SUS304 or from SUS304 to AA5083. This means that no compound with a uniform composition was formed. This agrees well with the SEM images in Figure 10. This can be explained by the mutual diffusion between AA5083 and SUS304. The ultimate thickness of the diffusion layer is ~2.31 μm, as shown in Figure 11c, which is comparable with the thickness of the IMCs in conventional VFSLW. This state can be regarded as the earlier stage of the IMCs. However, the significant diffusion is within 0.5 μm, as shown in Figure 11a–c.
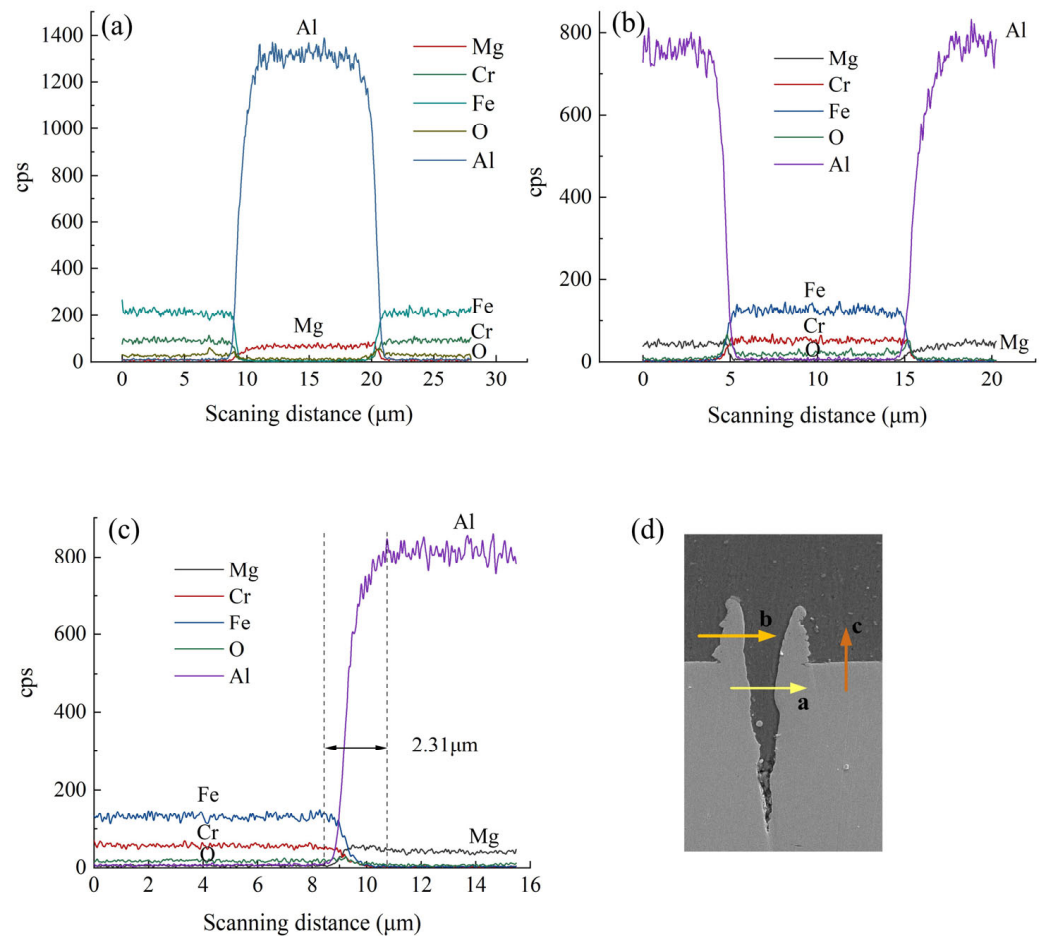
Figure 11. EDS linear scanning results of the Al/steel interfaces in MG-VFSLW: (**a**) across the steel rivet; (**b**) across the aluminum rivet; (**c**) across the straight Al/steel interface; (**d**) schematic of the linear scanning.

To find the difference between the riveting interface and the straight interface, the changes in the element content obtained by the EDS linear scanning across the interfaces in Figure 10c,d are shown in Figure 12. In Figure 12a, the interface is the straight interface, which was bonded by the original AA5083 plate and SUS304 plate directly. Using the visible boundary as a reference, it can be concluded that Al, Mg diffusing into SUS304 and Fe, Cr diffusing into AA5083 were simultaneous. An O-rich region on the boundary was seen, which further verified that the O element came from the oxides on the workpiece surface. However, in Figure 12b, on the riveting interface, mainly the Al and Mg diffusing into SUS304 was seen. The diffusion of Al is easy to understand because the Al atom can dissolve in iron. For the Mg element, although it does not dissolve in iron, it is easily captured by the O element. Therefore, it was also diffused into SUS304. Even an Mg-poor region was formed, as shown in Figure 12b. However, no obvious Mg-poor region formed on the straight interface in Figure 12a. This may be because the O content on the riveting interface was higher than that on the straight interface. This can be attributed to severe oxidation during laser ablation. The above results show that the vacuum environment is better for laser ablation pretreatment in MG-VFSLW. It is worth mentioning that no crack occurred in MG-VFSLW although the segregation of O and Mg was observed. This should be attributed to the weak segregation of Mg. The Mg atoms were not forced to gather significantly because the interdiffusion of Fe-Al in MG-VFSLW was weaker than that in VFSLW.
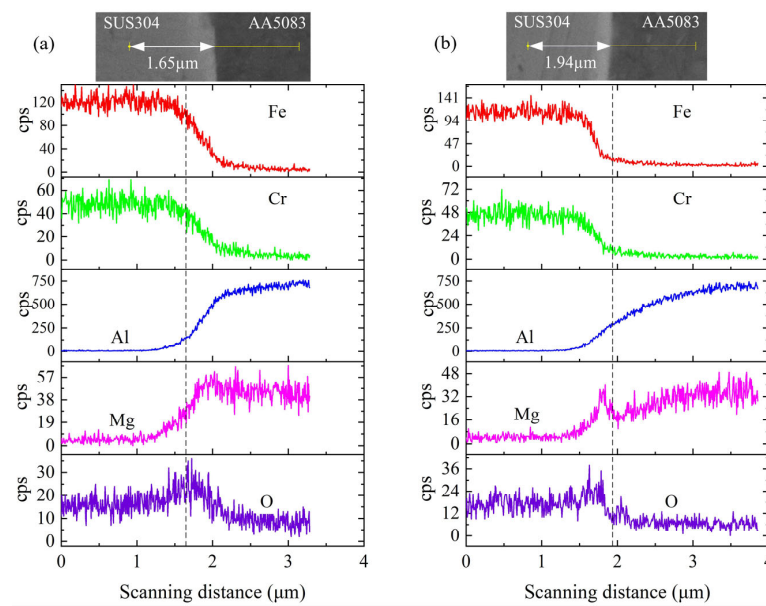
Figure 12. EDS linear scanning results across the Al/steel interface in MG-VFSLW: (**a**) the straight interface; (**b**) the riveting interface.

3.3. Mechanical Properties

3.3.1. Tensile Shear Test

Figure 13 shows the tensile shear load displacement curves of the joints obtained by conventional VFSLW and MG-VFSLW. It can be seen that the ultimate tensile shear loads of the joints with micro-grooves are large and uniform. The maximum value is close to 9 kN. The curves are also nearly overlapped, showing the stability of the MG-VFSLW joint quality. However, for the joints without micro-grooves, the tensile shear load displacement curves were very divergent. Both the elongation and the ultimate load ranged greatly among the three specimens. The average ultimate tensile shear load is only 6.24 kN, which is 2.51 kN lower than that of the MG-VFSLW joints. After the tensile shear test, the bending of the MG-VFSLW specimen was much larger than that of the VFSLW specimen, although both fracture locations were on the interface. These results showed that the assistance of the micro-grooves greatly improved the mechanical properties of the Al/steel dissimilar joint.
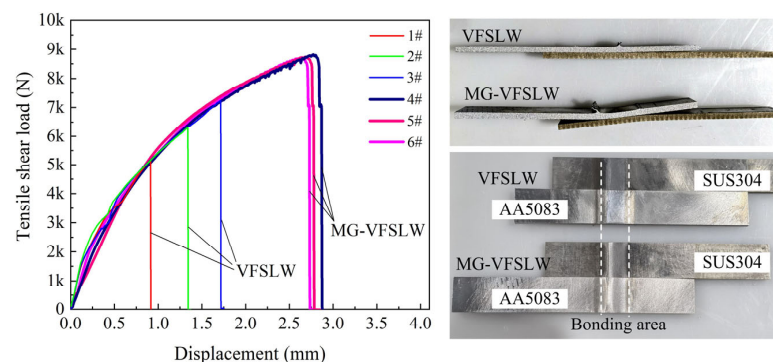
Figure 13. Tensile shear load displacement curves of VFSLW and MG-VFSLW joints and the typical specimens after the test.

Figure 14 summarizes some data about Al/steel lap joining according to published documents [7,34,36,45]. The tensile shear load was standardized by line load, which is defined as the ultimate tensile shear load divided by the width of the specimen. The line load of the conventional VFSLW joint obtained in this study is 346.8 N/mm. It increased to 485.9 N/mm by 40.1% in the MG-VFSLW joint, which is much higher than those in

laser welding–brazing (LW-B) [7], FSaFSLW [34], SR-FSLW [45], and UVeFSW [36]. This indicates that the MG-VFSLW process has great potential in Al/steel dissimilar joining.
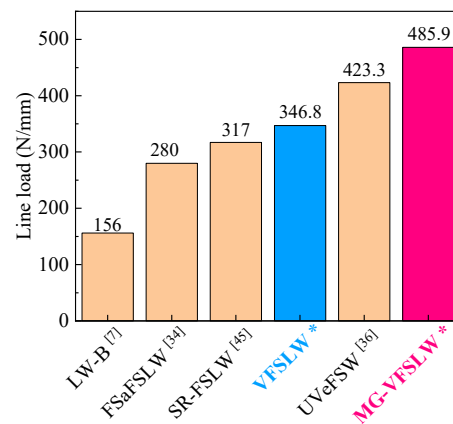
Figure 14. Standardized tensile shear strength of Al/steel lap joints obtained by various welding processes. Note: the symbol * means the data obtained in the current study. (LW-B) [7], FSaFSLW [34], SR-FSLW [45], and UVeFSW [36].

3.3.2. Microhardness Test

Figure 15 shows the microhardness distributions on the cross-section of the Al/steel joint. In the conventional VFSLW, on the AA5083 side, owing to the AA5083 aluminum alloy being a non-heat-treatable alloy, the microhardness parallel to the Al/steel interface hardly changed. However, the microhardness of the stir zone in MG-VFSLW increased slightly, as shown in Figure 15a. This may be caused by the decrease in the heat input in MG-VFSLW: owing to the existence of the micro-grooves, the plastic flow material will fill into the micro-grooves during the welding process, and thus the frictional pressure will decrease in MG-VFSLW. As a result, the heat generation rate decreased. On the SUS 304 side, the microhardness distributions in VFSLW and MG-VFSLW have no obvious difference, as shown in Figure 15b. This is because the welding temperature was too low and the dwell time was too short to soften the stainless steel.
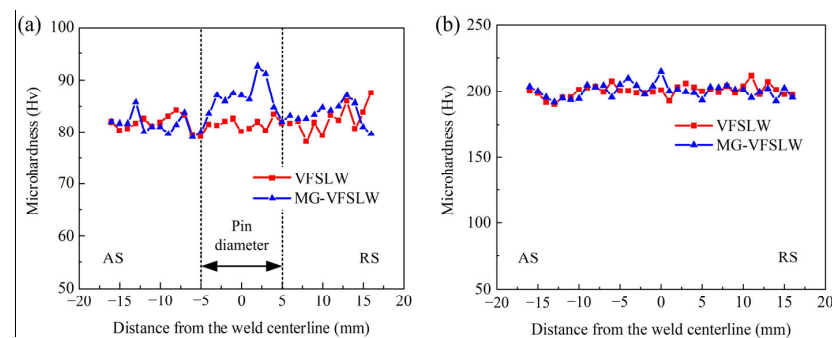
Figure 15. Microhardness distributions of the A/steel joint: (**a**) AA5083 side parallel to the interface; (**b**) SUS304 side parallel to the interface.

3.4. Failure Analysis

Figure 16 shows the fracture surface morphologies of the tensile specimen fabricated by conventional VFSLW. They were taken from the SUS304 side. The fracture surface included two typical regions, as shown in Figure 13. Near the edge of the bonding region, some bulks containing Al were found, as shown in Figure 16a,b. This region was inferred as the crack initiation region due to the stress concentration. Close to the center of the bonding region, the bulk-shaped Al was hardly seen. Meanwhile, some cleavage planes containing Al existed, as shown in Figure 16c,d. These features are the typical characteristics of brittle fractures. They are consistent with the tensile shear test results.
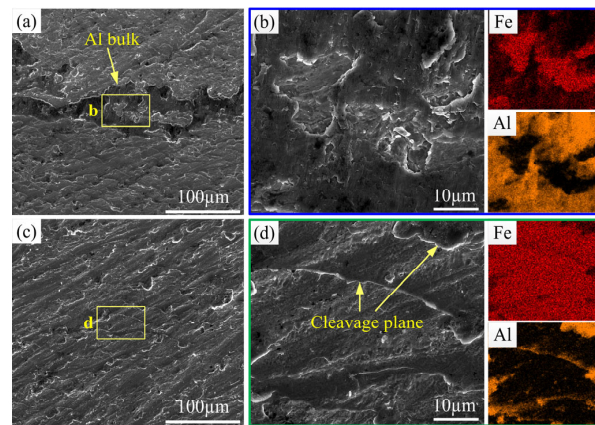
Figure 16. SEM images and the corresponding elements distribution maps of the fracture surface on SUS304 in VFSLW: (**a**) the crack initiation region; (**b**) the magnified figure of the area marked b; (**c**) the crack propagation region; (**d**) the magnified figure of the area marked d.

Figure 17 shows the fracture surface morphologies and the corresponding element distribution of the tensile specimen fabricated by MG-VFSLW, which were also taken from the SUS304 side. The overview figure of the fracture surface is shown in Figure 17a. It can be seen that the parallel-distributed micro-grooves remained on the fracture surface. Within the micro-grooves, AA5083 strips were found even though some cracks along the AA5083 strip were seen, as shown in Figure 17b. This means that the aluminum rivet was cut off during the tensile shear test, showing that the interface of the aluminum rivet was strong enough to bear the peak load during the tensile shear test. The mechanical interlock contributed significant strength to the Al/steel joint. In addition, in the direct bonding region between AA5083 and SUS304, some dimples and tearing ridges locally existed on the fracture surface. This shows some characteristics of the ductile fracture, which are also consistent with the tensile shear test results. These results show that the prefabricated micro-grooves improved the mechanical properties of the Al/steel joint not only by mechanical interlock but also by enhancing the direct bonding quality of Al/steel.
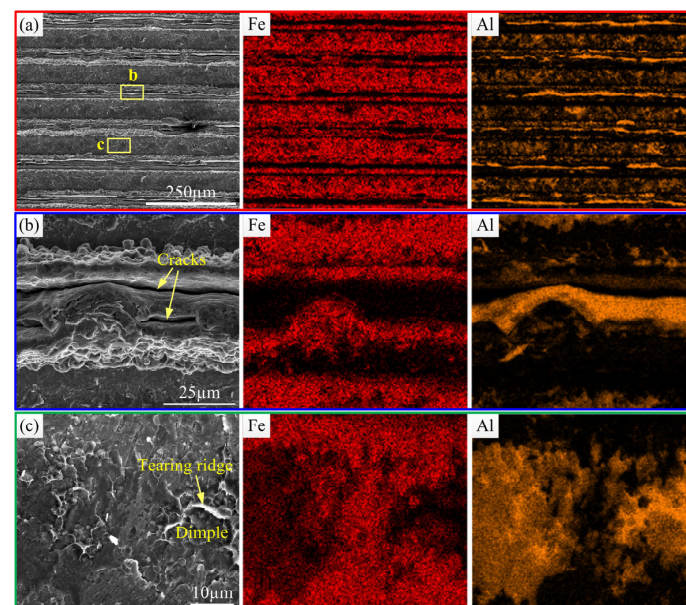
Figure 17. SEM images and the corresponding elements distribution maps of the fracture surface on the SUS304 side in MG-VFSLW: (**a**) the overview figure; (**b**) the interlocking region; (**c**) the direct bonding region.

4. Conclusions

In this study, a new Al/steel dissimilar joining method, i.e., the micro-groove-assisted vortex-friction stir lap welding process, was proposed. By comparing the weld formation, interface microstructure, and mechanical properties of the joints in MG-VFSLW with those in conventional VFSLW, the following conclusions can be drawn:

(1) Good Al/steel joint quality with a line load up to 485.9 N/mm was obtained by the MG-VFSLW process, which is higher than many other joining methods. Under the same welding conditions, the line load was only 346.8 N/mm in conventional VFSLW;

(2) Remarkable intermetallic compound layers and cracks were found in VFSLW. The thickness of the IMCs was 1.20 μm to 1.97 μm. The cracks were closely related to the oxides on the interface. However, they were eliminated by the laser ablation pretreatment in MG-VFSLW. The micro-grooves suppressed the formation of IMCs in MG-VFSLW, shown by no elemental step occurring on the line scanning images, which further suppressed the cracks caused by oxides;

(3) High-quality mechanical interlock was formed between AA5083 and SUS304 during the MG-VFSLW process, shown by the formation of aluminum rivets and steel rivets due to the micro-grooves and the flashes made by laser ablation. Sound metallurgical bonding was formed by diffusion on the riveting interface, the significant diffusion is within 0.5 μm, which further improved the strength of the mechanical interlock;

(4) The direct bonding quality between AA5083 and SUS304 was also improved by the micro-grooves due to the suppression of the IMCs' formation in MG-VFSLW. During the tensile shear tests, some dimples and tear ridges existed on the fracture surface of the direct bonding, showing the characteristics of ductile fracture.

Author Contributions: Conceptualization, X.L. and J.L.; methodology, X.L., J.L. and W.B.; software, X.L.; validation, X.L.; formal analysis, X.L.; investigation, X.L., J.L., W.B. and X.P.; resources, X.P., Q.W. and Z.N.; data curation, J.L. and W.B.; writing—original draft preparation, X.L.; writing—review and editing, X.L. and X.P.; visualization, X.L.; supervision, Z.N.; project administration, X.L.; funding acquisition, Z.N. All authors have read and agreed to the published version of the manuscript.

Data Availability Statement: Data will be made available on request.

References

1. Schubert, E.; Klassen, M.; Zerner, I.; Walz, C.; Sepold, G. Light-weight structures produced by laser beam joining for future applications in automobile and aerospace industry. *J. Mater. Process Technol.* **2001**, *115*, 2–8. [CrossRef]
2. Li, H.M.; Sun, D.Q.; Cai, X.L.; Dong, P.; Wang, W.Q. Laser welding of TiNi shape memory alloy and stainless steel using Ni interlayer. *Mater. Des.* **2012**, *39*, 285–293. [CrossRef]
3. Silvayeh, Z.; Domitner, J.; Sommitsch, C.; Hartmann, M.; Karner, W.; Götzinger, B. Mechanical properties and fracture modes of thin butt-joined aluminum-steel blanks for automotive applications. *J. Manuf. Process* **2020**, *59*, 456–467. [CrossRef]
4. Aceves, S.M.; Espinosa-Loza, F.; Elmer, J.W.; Huber, R. Comparison of Cu, Ti and Ta interlayer explosively fabricated aluminum to stainless steel transition joints for cryogenic pressurized hydrogen storage. *Int. J. Hydrogen Energy* **2015**, *40*, 1490–1503. [CrossRef]
5. Wang, G.; Zhao, Y.; Hao, Y. Friction stir welding of high-strength aerospace aluminum alloy and application in rocket tank manufacturing. *J. Mater. Sci. Technol.* **2018**, *34*, 73–91. [CrossRef]
6. Xia, H.; Li, L.; Tan, C.; Yang, J.; Li, H.; Song, W.; Zhang, K.; Wang, Q.; Ma, N. In situ SEM study on tensile fractured behavior of Al/steel laser welding-brazing interface. *Mater. Des.* **2022**, *224*, 111320. [CrossRef]
7. Yang, J.; Su, J.; Gao, C.; Zhao, Y.; Liu, H.; Oliveira, J.P.; Caiwang, T.; Zhishui, Y. Effect of heat input on interfacial microstructure, tensile and bending properties of dissimilar Al/steel lap joints by laser welding-brazing. *Opt. Laser Technol.* **2021**, *142*, 107218.
8. Peng, M.; Liu, H.; Liang, Y.; Xu, W.; Zhao, Y.; Chen, S.; Weng, J.; Yang, J. CMT welding-brazing of al/steel dissimilar materials using cycle-step mode. *J. Mater. Res. Technol.* **2022**, *18*, 1267–1280. [CrossRef]
9. Ye, Z.; Huang, J.; Cheng, Z.; Wang, S.; Yang, J.; Chen, S.; Zhao, X. Interfacial characteristics and mechanical properties of aluminum/steel butt joints fabricated by a newly developed high-frequency electric cooperated arc welding-brazing process. *J. Mater. Process Technol.* **2021**, *298*, 117317. [CrossRef]

10. Xu, P.; Hua, X.; Shen, C.; Mou, G.; Li, F. Formation of Fe_5Si_3 precipitate in the Fe_2Al_5 intermetallic layer of the Al/steel dissimilar arc welding joint: A transmission electron microscopy (TEM) study. *Mater. Character* **2021**, *178*, 111236. [CrossRef]

11. Wu, D.; Geng, W.; Li, H.; Wang, L.; Yu, K.; Sun, D. Interface characteristics and formation mechanism of plasma arc welding-brazing aluminum alloy/ultrahigh-strength steel joint. *Metall. Res. Technol.* **2021**, *118*, 405. [CrossRef]

12. Chen, S.; Li, S.; Li, Y.; Huang, J.; Chen, S.; Yang, J. Butt welding-brazing of steel to aluminum by hybrid laser-CMT. *J. Mater. Process Technol.* **2019**, *272*, 163–169. [CrossRef]

13. Wen, Z.; Yu, G.; Li, S.; Li, Y.; Chen, S.; Chen, S.; Huang, J.; Yang, J. Influence of Ni/Zn double coating on the steel on penetration welding-brazing by CMT arc-laser hybrid heat source. *Opt. Laser Technol.* **2021**, *134*, 106602. [CrossRef]

14. Singh, J.; Arora, K.S.; Shukla, D.K. Dissimilar MIG-CMT weld-brazing of aluminium to steel: A review. *J. Alloys Compd.* **2019**, *783*, 753–764. [CrossRef]

15. Jiang, H.; Liao, Y.; Gao, S.; Li, G.; Cui, J. Comparative study on joining quality of electromagnetic driven self-piecing riveting, adhesive and hybrid joints for Al/steel structure. *Thin Wall Struct.* **2021**, *164*, 107903. [CrossRef]

16. Deng, J.H.; Lyu, F.; Chen, R.M.; Fan, Z.S. Influence of die geometry on self-piercing riveting of aluminum alloy AA6061-T6 to mild steel SPFC340 sheets. *Adv. Manuf.* **2019**, *7*, 209–220. [CrossRef]

17. Haghshenas, M.; Gerlich, A.P. Joining of automotive sheet materials by friction-based welding methods: A review. *Eng. Sci. Technol.* **2018**, *21*, 130–148. [CrossRef]

18. Wang, H.; Qin, G.; Geng, P.; Ma, X. Interfacial microstructures and mechanical properties of friction welded Al/steel dissimilar joints. *J. Manuf. Process* **2020**, *49*, 18–25. [CrossRef]

19. Shirzadi, A.A.; Zhang, C.; Mughal, M.Z.; Xia, P. Challenges and latest developments in diffusion bonding of high-magnesium aluminium alloy (Al-5056/Al-5A06) to stainless steels. *Metals* **2022**, *12*, 1193. [CrossRef]

20. Khedr, M.; Hamada, A.; Järvenpää, A.; Elkatatny, S.; Abd-Elaziem, W. Review on the Solid-State Welding of Steels: Diffusion Bonding and Friction Stir Welding Processes. *Metals* **2022**, *13*, 54. [CrossRef]

21. Chu, Q.; Xia, T.; Zhao, P.; Zhang, M.; Zheng, J.; Yan, F.; Cheng, P.; Yan, C.; Liu, C.; Luo, H. Interfacial investigation of explosion-welded Al/steel plate: The microstructure, mechanical properties and residual stresses. *Mater. Sci. Eng. A* **2022**, *833*, 142525. [CrossRef]

22. Wan, L.; Huang, Y. Friction stir welding of dissimilar aluminum alloys and steels: A review. *Int. J. Adv. Manuf. Technol.* **2018**, *99*, 1781–1811. [CrossRef]

23. Shen, Z.; Ding, Y.; Chen, J.; Amirkhiz, B.S.; Wen, J.; Fu, L.; Gerlich, A. Interfacial bonding mechanism in Al/coated steel dissimilar refill friction stir spot welds. *J. Mater. Sci. Technol.* **2019**, *35*, 1027–1038. [CrossRef]

24. Jabraeili, R.; Jafarian, H.R.; Khajeh, R.; Park, N.; Kim, Y.; Heidarzadeh, A.; Eivani, A.R. Effect of FSW process parameters on microstructure and mechanical properties of the dissimilar AA2024 Al alloy and 304 stainless steel joints. *Mater. Sci. Eng. A* **2021**, *814*, 140981. [CrossRef]

25. Ramachandran, K.K.; Murugan, N.; Kumar, S.S. Effect of tool axis offset and geometry of tool pin profile on the characteristics of friction stir welded dissimilar joints of aluminum alloy AA5052 and HSLA steel. *Mater. Sci. Eng. A* **2015**, *639*, 219–233. [CrossRef]

26. Wang, T.; Komarasamy, M.; Liu, K.; Mishra, R.S. Friction stir butt welding of strain-hardened aluminum alloy with high strength steel. *Mater. Sci. Eng. A* **2018**, *737*, 85–89. [CrossRef]

27. Dehghani, M.; Amadeh, A.; Mousavi, S.A.A.A. Investigations on the effects of friction stir welding parameters on intermetallic and defect formation in joining aluminum alloy to mild steel. *Mater. Des.* **2013**, *49*, 433–441. [CrossRef]

28. Pourali, M.; Abdollah-zadeh, A.; Saeid, T.; Kargar, F. Influence of welding parameters on intermetallic compounds formation in dissimilar steel/aluminu friction stirwelds. *J. Alloys Compd.* **2017**, *715*, 1–8. [CrossRef]

29. Liu, X.; Lan, S.H.; Ni, J. Analysis of process parameters effects on friction stir welding of dissimilar aluminum alloy to advanced high strength steel. *Mater. Des.* **2014**, *59*, 50–62. [CrossRef]

30. Saleh, M.; Liu, H.; Ushioda, K.; Fujii, H. Effect of Zn interlayer on friction stir butt welding of A1100 and SUS316L stainless steel. *Sci. Technol. Weld Join* **2022**, *27*, 361–373. [CrossRef]

31. Zhang, M.; Wang, Y.; Xue, P.; Zhang, H.; Ni, D.; Wang, K.S.; Ma, Z. High-quality dissimilar friction stir welding of Al to steel with no contacting between tool and steel plate. *Mater. Character.* **2022**, *191*, 112128. [CrossRef]

32. Wei, Y.; Li, J.; Xiong, J.T.; Zhang, F.S. Effect of tool pin insertion depth on friction stir lap welding of aluminum to stainless steel. *J. Mater. Eng. Perform.* **2013**, *22*, 3005–3013. [CrossRef]

33. Wan, L.; Huang, Y. Microstructure and mechanical properties of Al/steel friction stir lap weld. *Metals* **2017**, *7*, 542. [CrossRef]

34. Zhou, L.; Yu, M.; Liu, B.; Zhang, Z.; Liu, S.; Song, X.; Zhao, H. Microstructure and mechanical properties of Al/steel dissimilar welds fabricated by friction surfacing assisted friction stir lap welding. *J. Mater. Res. Technol.* **2020**, *9*, 212–221. [CrossRef]

35. Huang, Y.; Wan, L.; Si, X.; Huang, T.; Meng, X.; Xie, Y. Achieving high-quality Al/steel joint with ultrastrong interface. *Metall. Mater. Trans. A* **2019**, *50*, 295–299. [CrossRef]

36. Liu, T.; Gao, S.; Ye, W.; Shi, L.; Kumar, S.; Qiao, J. Achievement of high-quality joints and regulation of intermetallic compounds in ultrasonic vibration enhanced friction stir lap welding of Aluminum/Steel. *J. Mater. Res. Technol.* **2023**, *25*, 5096–5109. [CrossRef]

37. Wang, X.; Lados, D.A. Optimization of aluminum-to-steel friction stir lap welding for the fabrication of high-integrity structural components. *J. Adv. Join Process.* **2022**, *5*, 100114. [CrossRef]

38. Liu, F.; Zhang, Y.; Dong, P. Large area friction stir additive manufacturing of intermetallic-free aluminum-steel bimetallic components through interfacial amorphization. *J. Manuf. Process.* **2022**, *73*, 725–735. [CrossRef]

39. Liu, F.; Dong, P.; Khan, A.; Sun, K.; Lu, W.; Taub, A.; Allison, J. Amorphous interfacial microstructure and high bonding strength in Al-Fe bimetallic components enabled by a large-area solid-state additive manufacturing technique. *J. Mater. Process. Technol.* **2022**, *308*, 117721. [CrossRef]

40. Luo, J.; Zhou, Y.; Liu, X.; Jia, L. Vortex-friction stir lap welding of 5083 aluminum alloy/304 stainless steel dissimilar materials. *Electr. Weld. Mach.* **2023**, *53*, 62–71. (In Chinese)

41. Liu, X.; Zhen, Y.; Shen, Z.; Chen, H.; Li, W.; Guo, W.; Yue, Z. A modified friction stir welding process based on vortex material flow. *Chin. J. Mech. Eng.* **2020**, *33*, 90. [CrossRef]

42. Liu, X.; Sun, Z. Numerical simulation of vortex-friction stir welding based on internal friction between identical materials. *Int. J. Heat Mass Transfer* **2022**, *185*, 122418. [CrossRef]

43. Liu, X.; Li, W.; Zhen, Y.; Jia, L.; Li, Y.; Pei, X. Effect of process parameters on weld quality in vortex-friction stir welding of 6061-T6 aluminum alloy. *Materials* **2023**, *16*, 873. [CrossRef] [PubMed]

44. Liu, X.; Wang, Q.; Pei, X.; Li, Y.; Zhen, Y.; Shen, Z.K.; Chen, H. Microstructural evolution of 6061-T6 aluminum alloy in vortex-friction stir welding. *Mater. Character.* **2023**, *195*, 112544. [CrossRef]

45. Huang, Y.; Huang, T.; Wan, L.; Meng, X.; Zhou, L. Material flow and mechanical properties of aluminum-to-steel self-riveting friction stir lap joints. *J. Mater. Process. Technol.* **2019**, *263*, 129–137. [CrossRef]

46. Elrefaey, A.; Gouda, M.; Takahashi, M.; Ikeuchi, K. Characterization of aluminum/steel lap joint by friction stir welding. *J. Mater. Eng. Perform.* **2005**, *14*, 10–17. [CrossRef]

47. Sahu, M.; Paul, A.; Ganguly, S. Influence of frictional heat spread pattern on the formation of intermetallic layers at the dissimilar FSW joint interface between AA 5083 and HSLA steel. *J. Manuf. Process.* **2022**, *83*, 555–570. [CrossRef]